Title

Tandem LIM domain-containing proteins, LIMK1 and LMO1, directly bind to force-bearing keratin intermediate filaments

Journal

Cell Reports, 43(7)

ISSN

2639-1856

Authors

Kim, Dah Som

Cheah, Joleen S

Lai, Tzu Wei

et al.

Publication Date

2024-07-01

DOI

10.1016/j.celrep.2024.114480

Peer reviewed

HHS Public Access

Author manuscript

Cell Rep. Author manuscript; available in PMC 2024 December 02.

Published in final edited form as:

Cell Rep. 2024 July 23; 43(7): 114480. doi:10.1016/j.celrep.2024.114480.

Tandem LIM domain-containing proteins, LIMK1 and LMO1, directly bind to force-bearing keratin intermediate filaments

Dah Som Kim[1,6], **Joleen S. Cheah**[1,4,6], **Tzu Wei Lai**[1], **Karen X. Zhao**[1,5], **Skylar R. Foust**[1], **Yuh-Ru Julie Lee**[2], **Su Hao Lo**[3], **Volkmar Heinrich**[1], **Soichiro Yamada**[1,7,*]

[1]Biomedical Engineering Department, University of California, Davis, Davis CA 95616, USA

[2]Department of Plant Biology, University of California, Davis, Davis CA 95616, USA

[3]Department of Biochemistry and Molecular Medicine, University of California, Davis, Davis CA 95616 USA

[4]Present address: Biosciences Program, Stanford University, Stanford, CA 94305, USA

[5]Present address: Biomedical Sciences, University of California, Riverside, Riverside, CA 92521, USA

[6]These authors contributed equally

[7]Lead contact

SUMMARY

The cytoskeleton of the cell is constantly exposed to physical forces that regulate cellular functions. Selected members of the LIM (Lin-11, Isl-1, and Mec-3) domain-containing protein family accumulate along force-bearing actin fibers, with evidence supporting that the LIM domain is solely responsible for this force-induced interaction. However, LIM domain's force-induced interactions are not limited to actin. LIMK1 and LMO1, both containing only two tandem LIM domains, are recruited to force-bearing keratin fibers in epithelial cells. This unique recruitment is mediated by their LIM domains and regulated by the sequences outside the LIM domains. Based on *in vitro* reconstitution of this interaction, LIMK1 and LMO1 directly interact with stretched keratin 8/18 fibers. These results show that LIM domain's mechano-sensing abilities extend to the keratin cytoskeleton, highlighting the diverse role of LIM proteins in force-regulated signaling.

Graphical abstract

*Correspondence: syamada@ucdavis.edu.

AUTHOR CONTRIBUTIONS

Conceptualization, D.S.K., J.S.C., and S.Y.; investigation, D.S.K., J.S.C, T.W.L., K.X.Z., S.R.F., Y.-R.J.L., and S.Y.; writing – original draft, D.S.K., J.S.C., and S.Y.; writing – review & editing, D.S.K., J.S.C., and S.Y.; funding acquisition, J.S.C., T.W.L., K.X.Z., S.R.F., S.H.L., V.H., and S.Y.; resources, Y.-R.J.L., S.H.L., V.H., and S.Y.; supervision, Y.-R.J.L., S.H.L., V.H., and S.Y.

SUPPLEMENTAL INFORMATION

Supplemental information can be found online at https://doi.org/10.1016/j.celrep.2024.114480.

DECLARATION OF INTERESTS

The authors declare no competing interests.

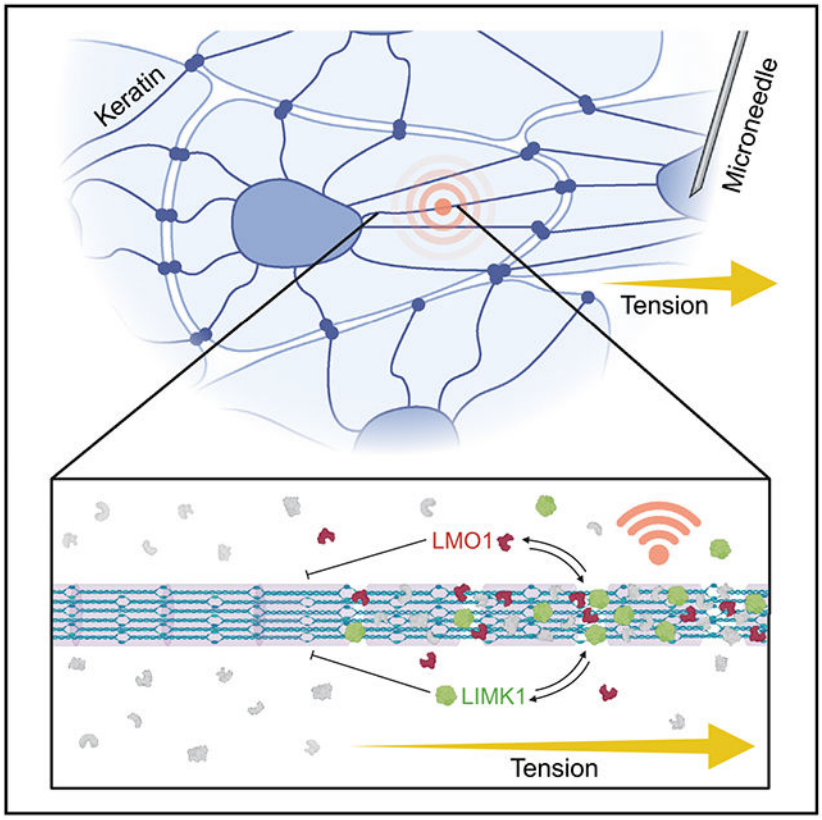

In brief

Kim et al. show that LIMK1 and LMO1, with two tandem LIM domains, directly bind to force-bearing keratin filaments in epithelial cells. The dynamic nature of this unique recruitment suggests their potential involvement in downstream signaling cascades originating from the keratin cytoskeleton, acting as a signaling hub.

INTRODUCTION

Epithelial tissues are constantly exposed to physical forces from neighboring cells. Cytoskeletal components and adhesive contacts are thought to provide the structural integrity necessary for tissue homeostasis and reorganization. Thus, force-dependent signaling, especially in regulating the cytoskeleton, has emerged as an integral part of signal transduction. Previous studies have implicated LIM (Lin-11, Isl-1, and Mec-3) domain-containing proteins as mechano-sensing proteins. All members of this protein family contain at least one domain of two tandem zinc-binding motifs/fingers that modulate protein interactions.[1,2] However, apart from the zinc-coordinating cysteine and histidine residues conserved in the LIM domains, the sequence within these domains exhibits considerable diversity, thus interacting with various binding partners. This is also reflected in the wide range of localizations exhibited by the protein members, with some associating with focal adhesions, some binding to actin filaments, and others residing in the nucleus, acting as transcriptional regulators, suggestive of their functional diversity. Therefore, investigating

the specific mechano-responses of these LIM proteins will generate insights into each proteins' specific function and help develop a comprehensive picture of the role of the protein family as a whole in mechano-transduction.

The force dependence of selected LIM proteins is well documented in contractile stress fibers and focal adhesions in fibroblasts.[3,4] For example, zyxin and paxillin LIM proteins have been observed to re-localize along actin fibers or focal adhesions in response to physical perturbations generated using atomic force microscopy,[5,6] a glass microneedle,[7] shear flow,[8] and substrate stretch[8–11] as well as along cell-cell contacts using substrate stretch.[12] Additionally, zyxin and paxillin LIM proteins have been demonstrated to accumulate along contractile actin fibers at spontaneous strain sites[13,14] when induced by activating RhoA[15] or partial laser ablation of actin stress fibers[5,16] (also observed in the testin LIM protein[17]). Zyxin, with its three LIM domains in particular, is recruited to focal adhesions in a force-dependent manner[18] to regulate the dynamics of actin[10] and focal adhesion[19] and accumulates along tensed actin fibers to repair damaged filaments.[14]

Recent studies identified several key requirements for LIM proteins' unique force sensitivity. For example, LIM proteins require at least three consecutive LIM domains for efficient recruitment to force-bearing actin fibers.[11,16] Furthermore, both studies demonstrated the direct binding between zyxin's LIM domains and "tensed" actin filaments *in vitro*.[11,16] Unlike fibroblast models that were used in previous studies, in this study, an epithelial cell model was used to screen 18 different LIM proteins across the 14 classes in the protein family. This uncovered surprising interactions between LIM proteins and the cyto-keratin network unique to epithelial cells.

RESULTS

To test the force-induced recruitment of LIM domain-containing proteins, epithelial MDCK (Madin-Darby canine kidney) cells expressing GFP-tagged LIM proteins were mechanically stimulated by a microneedle placed on adjacent neighboring cells. Using a micro-manipulator, the microneedle was moved away from the expressing cell, thus exposing the expressing cell to mechanical strain via cell-cell contacts (Figures 1 and S1). The movement of the microneedle was manually controlled to ensure consistent pulling of cells, which often varied depending on cell confluency and size as well as the stability of microneedle attachment to the cell (Figure S1G). However, the stretch-induced protein accumulation was relatively insensitive to the loading rate (Figures S1G–S1I).

We chose at least one representative protein from each class of the LIM protein family for the screen (Figure S1A), and generally, our results were consistent with previous studies[11,16]: the force-induced accumulation was observed in most LIM proteins containing three or more LIM domains, with an exception of PINCH (Figures 1B, S1C, and S1D). The LIM proteins with a single LIM domain (PDLIM1, EPLINα, LASP1, and ZNF185) accumulated along fibrous structures to varying degrees (Figures 1B, S1C, and S1D). Note that, while these proteins have been shown to interact with actin filaments (EPLINα, LASP1, and ZNF185[20–22]) and α-actinin (PDLIM1[23,24]), the interactions are attributed to the sequences outside of the LIM domain, and these proteins are likely recruited to

newly repaired actin fibers by zyxin and other proteins.[14] Consistently, the isolation of LIM domain from these proteins abolished fiber accumulation (Figure S1E).

Among LIM proteins containing two LIM domains, LIMK1 and LMO1 accumulated along fibrous structures, albeit weakly compared to zyxin, which contains three tandem LIM domains (Figures 1A and 1B), while ISL1 and CRIP2 did not (Figures 1B, S1C, and S1D). Typically, truncating of zyxin's three LIM domains down to two significantly reduces zyxin's force-induced accumulation.[16,18] Therefore, we suspected that this stretch-induced interaction may be due to the sequences outside the LIM domains of LIMK1 and LMO1. For example, LIMK1 regulates actin dynamics by phosphorylating cofilin,[25] and its association with the actin filaments may be independent of the LIM domains. Surprisingly, however, the LIM domains alone from both LIMK1 and LMO1 were recruited to the fibrous structures in cells (Figures 2A, 2B, and 2D). Furthermore, the LIM domains alone of LMO1 accumulated to a similar extent as the LIM domains of zyxin (Figure S1E). This is contrary to the three tandem LIM domain principle for force-induced accumulation along tensed actin filaments.[11,16]

Interestingly, stretch-induced LIMK1- and LMO1-positive fibers were dissimilar to those of other LIM proteins, and these fibers often terminated at cell-cell contacts, while zyxin-positive actin filaments are often observed away from cell-cell contacts (Figure 1A; Videos S1, S2, and S3). This resembled the keratin network rather than the actin cytoskeleton. For example, representative LIM proteins with positive fibrous accumulation (PDLIM7, zyxin, ABLIM2, paxillin, and FHL2) co-localized with F-tractin, a marker for actin filaments, except for LIMK1 and LMO1 (Figure 1C). Instead, LIMK1 and LMO1 co-localized with keratin 18 filaments, whereas other LIM proteins did not (Figure 1C). The force-sensitive nature of selected LIM proteins thus far has been implicated in actin filament regulation, whereas cten, a member of the tensin family, has been shown to localize to the force-bearing keratin fibers.[26] We used cten as a proxy to isolate the strained keratin fibers from the dense network of keratin filament in epithelial cells. Indeed, LIMK1 and LMO1 co-localized with cten, rather than zyxin, upon cell stretch (Figures 1D and 1E). Since the keratin network is independent of the actin cytoskeleton, cten was recruited to the keratin fibers regardless of cytochalasin D addition (Figure S2A), whereas for paxillin, a LIM protein with four LIM domains, recruitment was severely diminished upon cytochalasin addition (Figure S2A). Consistent with cten's recruitment to keratin filaments, LIMK1 and LMO1 recruitment to these fibers was also cytochalasin D independent (Figures S2B and S2C), indicating that these fibers are not actin filament but, rather, keratin fibers; see additional evidence using keratin 8 knockout cells below.

LIMK1 contains tandem LIM domains at the N terminus and a kinase domain at the C terminus (Figure 2A). The deletion of the LIM domains from LIMK1 (LIMK1ΔLIM) significantly reduced force-induced accumulation, while the tandem LIM domains alone were sufficient to reproduce accumulation of a similar extent as the full-length protein (Figure 2B). The LIM domains of LIMK1 bind and inhibit the C-terminal kinase domain,[27,28] which may explain why LIM deletion did not completely eliminate force-induced accumulation of LIMK1ΔLIM due to a possible interaction with endogenous LIMK1. Interestingly, the LIMK1 LIM domain alone was recruited to the nucleus,

consistent with the previous finding that LIMK1 localized predominantly to the nucleus in the absence of the PDZ (post synaptic density protein, *Drosophila* disc large tumor suppressor, and zonula occludens-1 protein) domain.[29] This nuclear translocation may be a part of mechano-induced signaling, reminiscent of FHL (four and a half LIM domains) protein.[11]

We hypothesize that phosphorylation sites outside the LIM domains may regulate this auto-inhibition and LIMK1-LIM domains' force-sensitivity. We sought to disrupt this interaction by substituting the serine at position 323, known to be phosphorylated by MAPKAPK-2 to regulate cell migration,[30] and the serine at position 337, preferentially phosphorylated in mitotic cells,[31] with either alanine (non-phosphorylated) or glutamic acid (phospho-mimetic). Note that, since the differences in force-induced accumulation of LIMK1 mutants were subtle, we did not include cytoskeletal markers (zyxin or cten) to minimize any potential competition from these proteins.

While all phospho-mutants were force sensitive and relocalized along the fibers upon cell stretch, similar to wild-type LIMK1, the S337E phospho-mimetic mutant had a significant increase in force-induced accumulation over the wild-type LIMK1 protein (Figure 2C). This improvement in force-induced recruitment was independent of LIMK1's kinase activity, as the kinase-dead mutant (D460A) had no effect on force-induced recruitment to fibers (Figure 2C). Therefore, LIMK1 is similar to testin, a LIM protein with a latent mechano-sensitivity,[17] in that phosphorylation may play a role in its force-dependent dynamics. This raises the intriguing possibility that, during mitosis, where the keratin filaments undergo re-organization, in part aided by its phosphorylation,[32] the sensitivity of force-induced interaction between LIMK1-keratin fibers may be elevated and facilitate mechano-transduction initiated by forces from drastic cell shape changes in mitosis.

In contrast to LIMK1 with a well-known kinase function outside its LIM domain, LMO1 is a tandem LIM protein with its LIM domain flanked by very short 23- and 15-amino acid sequences at the N and C terminus, respectively (Figure 2D). While the full-length LMO1 exhibited rather weak fiber localization upon cell stretch, the LIM domain of LMO1 responded more robustly to cell stretch (Figure 2D and S1E). Thus, the N-and/or C-terminal sequences likely auto-inhibit LMO1's force-sensitivity. In addition, single LIM domains (denoted as a and b) in LMO1 had reduced force-induced accumulation compared to LMO1's tandem LIM domains (Figure 2D), suggesting that, like other actin-binding LIM proteins, consecutive LIM domains are essential for this force-induced response of LMO1. This synergistic binding by tandem LIM domains is observed with Lbp1 and the LIM domains of LMO4, another member of the LMO protein family.[33] Interestingly, LMO1 is implicated in cancer, albeit as a transcriptional regulator,[34] and its force dependency and interaction with the keratin network have not been reported previously.

Since the LIMK1-S337E mutant and the tandem LIM domains of LMO1 (LMO1-LIM) had the most robust force-induced accumulation (Figures 2C and 2D), these mutants were used to assay for co-localization with zyxin, cten, and keratin 18 (Figure S3). Similar to the full-length proteins (Figures 1D and 1E), the LIMK1-S337E- and LMO1-LIM-positive fibers better correlated with cten than zyxin (Figures S3A, S3B, S3D, and S3E). Furthermore,

LIMK1-S337E and LMO1-LIM also localized to keratin 18 fibers (Figures S3C and S3F), though not all keratin fibers co-localized with LIMK1-S337E and LMO1-LIM, likely because only a subset of keratin fibers was under strain from cell stretch. Moreover, in keratin 8 knockout cells expressing GFP-tagged LIMK-S337E or GFP-tagged LMO-LIM, both LIMK1-S337E and LMO1-LIM exhibited minimal fibrous accumulation (Figures S2D and S2E), further demonstrating that keratin filaments are the responsible cytoskeletal component for LIMK1 and LMO1 binding. Note that this force-induced accumulation of LIMK1 and LMO1 was independent of calcium signaling, as the addition of EGTA or thapsigargin had no noticeable change in the accumulation (Figures S2F–S2G).

We sought to test whether LIMK1 and LMO1 bind directly or indirectly to force-bearing keratin fibers. Purified keratin 8 and 18 proteins (Figure 3A) were assembled into filaments and bundles and adsorbed onto a clean dish. When purified GFP-tagged LIMK1-S337E and LMO1-LIM proteins were added to the keratin bundles in the absence of strain, the LIM proteins did not accumulate along the keratin filaments (Figures 3A–3C). Subsequently, the keratin fibers were stretched using a microneedle, similar to the live-cell analysis. The tip of the microneedle slid under or pushed the sides of keratin fibers and detached a region of the keratin fibers from the surface while the remainder of the bundle stayed adhered to the surface, thereby providing anchoring points (Figure 3D). The microneedle moved laterally to stretch the fibers into a triangular profile, thus providing the quantification of non-stretch control and stretch regions along the same filament bundle (Figure 3D). Neither GFP nor the GFP-tagged tri-LIM domain from zyxin bound to keratin fibers at all strain levels applied to the keratin fibers (Figures 3D and 3F).

In contrast, GFP-LIMK1 S337E mutant, selected for its significantly increased force sensitivity from the live cell analysis (Figure 2C), accumulated to the stretched regions of the keratin network (Figure 3E, 3F, and S4). Strikingly, LIMK1 accumulation increased with higher magnitudes of stretch beyond ~20% strain (Figures 3E and 3F; Video S4), suggesting that there is a shift in protein conformation of keratin filaments at this threshold, facilitating LIMK1 binding. Moreover, the GFP signal of LIMK1 accumulation was observed extending outward from the keratin bundle (Figure 3F, green arrow). While these LIMK1-positive fibers initially appear to be independent of keratin bundles, high-contrast imaging shows that there was the presence of a keratin network adjacent to the large bundle and co-localized with LIMK1 (Figure S4A). These very fine keratin fibers were often deposited on the surface of the coverslips, often obscured by the keratin bundles with much higher staining (Figure S4B). As the microneedle laterally displaced the large keratin bundle, these fine keratin networks also stretched and, in some instances, tore, revealing the bare surface of the glass coverslip (Figure S4B). LIMK1 accumulation was also observed along the strained mesh-like keratin network (Figure S4B; see also Figure S4C for an LMO1 example), suggesting that the large bundle structure is not necessary for this recruitment.

Similar to LIMK1-S337E, GFP-tagged tandem LIM domains from LMO1 that co-localized with keratin fibers in live cells (Figure 2E) selectively and directly bound to the force-bearing keratin bundles *in vitro* (Figure 3F and S4C). For quantitative comparison of force-activated keratin binding among LIM proteins, we evaluated the intensity ratios of the GFP signals from GFP alone or GFP-tagged LIM proteins to the His tag fluorescence

signal from keratin fibers under low strain (<26% stretch) and under high strain (>26% stretch) (Figure 3F). Both LIMK1 and LMO1 accumulation to stretched keratin fibers were significantly greater than those of GFP and zyxin at all strain levels. Furthermore, both LIMK1-S337E and LMO1-LIM bound to keratin fibers more intensely at higher strains (Figure 3F), demonstrating that force-activated protein recruitment along the keratin fibers is strain dependent. These results are consistent with our live-cell data and suggest that LIM sequences are not limited to interacting with force-bearing actin fibers but can also interact with the keratin network in a force-dependent manner.

While the interaction between LIMK1/LMO1 and keratin fibers is direct and sensitive to force, the specific role of the LIMK1/LMO1-keratin fiber association remains unclear. Intermediate filaments, like keratin filaments, can withstand significant deformation, but they may need additional proteins to maintain their structure under large strain, similar to how zyxin helps repair strained actin filaments.[14] We aimed to determine whether LIMK1 and LMO1 provide structural support to the keratin cytoskeleton, possibly by binding to protect the strained fibers. This would necessitate their stable association with the keratin fibers. To test this hypothesis, we analyzed the fluorescence recovery of LIMK1 and LMO1 along strained keratin fibers both *in vitro* and in live cells.

Keratin 8/18 filaments, prepared *in vitro*, were stretched using a microneedle. Small regions of LIMK1-S337E and LMO1-LIM accumulation along the stretched keratin bundles were photobleached, and their recovery was monitored (Figures 4A and 4B). Similarly, MDCK cells expressing GFP-tagged LIMK1-S337E or LMO1-LIM were stretched, and the areas along the keratin network where the LIM proteins were bound were irreversibly photobleached. We then monitored the fluorescence recovery (Figures 4A and 4B). Notably, the recovery rate of LIMK1-S337E was significantly faster in live cells compared to *in vitro* (as shown in Figures 4C and 4G), which suggests a faster turnover in live cells.

Furthermore, GFP-tagged LMO1-LIM exhibited both higher-mobility fractions and significantly faster recovery rates in live cells compared to *in vitro* (Figures 4D–4G), similar to those of LIMK1, albeit with higher-mobility fractions. In contrast, keratin filaments have been shown to be highly stable structures with minimal subunit turnover in live cells.[35–37] Taken together, our data suggest that LIMK1 and LMO1 are more dynamic compared to the keratin network, raising the possibility that at least some fractions of LIMK1 and LMO1 are involved in downstream signaling pathways of mechano-transduction rather than serving a purely structural role.

DISCUSSION

While actin filaments attract diverse actin-binding proteins under mechanical stress,[38–40] little is known about force-induced recruitment of proteins surrounding intermediate filaments. In this study, we discovered that keratin filaments in cells and reconstituted keratin filament bundles directly recruit mechanosensing proteins, LIMK1 and LMO1, upon application of strain, similar to cten.[26] The keratin filaments may harbor cryptic binding sites for mechano-sensing proteins that are exposed under tension. In line with this idea, intermediate filaments, such as keratin and vimentin, have been suggested to undergo

conformational changes upon stretch,[41–44] which may be the mechanism by which the hidden binding sites are revealed.

Cells can survive large deformations, and intermediate filaments are crucial for this survival.[45,46] Due to the minimum number of intermediate filament-binding proteins discovered so far and the remarkable mechanical strength of intermediate filaments, it is thought that the intrinsic structural robustness of intermediate filaments is sufficient for cell survival. However, the recruitment of signaling proteins (LIMK1, LMO1, and Solo[47]) to keratin fibers and the transient nature of its interactions suggest that the keratin network may play a more active role in cells' mechano-resilience by acting as a signaling hub in mechano-transduction. In fact, the keratin network may serve as a better scaf-fold for force-sensitive signaling because, unlike actin filaments and microtubules, the intermediate filament network can withstand more extreme strains without breaking.[48] Given the previously limited number of proteins known to bind to the keratin network and the technical challenges in identifying force-induced protein interactions, there may be a broader spectrum of protein interactions surrounding the keratin network that play essential roles in mechano-transduction.

Limitations of the study

There are some limitations to this study that must be acknowledged. While we have conclusively demonstrated that mechanical force can induce LIMK1/LMO1-keratin filament interactions both in live cells and *in vitro*, our current microneedle-based cell stretch analysis lacks quantification of forces that are exerted on the keratin fibers in cells or purified keratin filaments, preventing the direct comparison between the live cell and *in vitro* systems. Moreover, based on our fluorescence recovery after photobleaching (FRAP) analysis, we suggest that LIMK1 and LMO1 may play signaling roles, but we cannot exclude the possibility that some immobile fractions of LIMK1 and LMO1 could stabilize the strained keratin filaments. Our work lays the groundwork for future studies on the structural details as well as the physiological implication of these unique force-dependent interactions on the keratin cytoskeleton.

STAR★METHODS

RESOURCE AVAILABILITY

Lead contact—Further information and requests for resources and reagents should be directed to and will be fulfilled by the Lead Contact, Soichiro Yamada (syamada@ucdavis.edu).

Materials availability—Plasmids generated in this study are available from the lead contact upon reasonable request.

Data and code availability

- All data reported in this paper will be shared by the lead contact upon reasonable request.

- All custom codes used in data analysis are available from the lead contact upon reasonable request.
- Any additional information required to reanalyze the data reported in this work paper is available from the lead contact upon request.

EXPERIMENTAL MODEL AND STUDY PARTICIPANT DETAILS

MDCK (Madin-Darby Canine Kidney) GII cells (female) were cultured at 37°C, 5% CO_2 in DMEM(Gibco) supplemented with 10% fetal bovine serum (FBS – RD Biosciences) and antibiotics. The cell line was checked for mycoplasma and routinely treated with mycoplasma removal agent (MRA) for preventive maintenance.

METHOD DETAILS

Plasmids, cloning, and transient transfection—Cells were transiently transfected with plasmids using Lipofectamine 3000 (Invitrogen) or jetOPTIMUS (Polyplus) according to the manufacturer's protocol. MDCK cells with keratin 8 knockout was described previously.[26] All genes were purchased from either Harvard PlasmID Database or Addgene (see key resources table for details), and subcloned into pEGFP-C1 vector (Invitrogen) using a Gibson assembly kit (NEB) with EcoRI and KpnI as restriction sites. GFP-tagged zyxin and zyxin-LIM1-3 (amino acids 338–572), paxillin, and trip6 were gifts from Dr. Masahiro Sokabe (Nagoya University, Japan), Dr. Christopher Turner (SUNY Upstate Medical University), and Dr. Dannel McCollum (University of Massachusetts), respectively.

Keratin 8/18 purification—Recombinant keratin 8 with His-tag and keratin 18 genes were inserted into pET vector and expressed separately in Lemo21(DE3) (NEB). The primers used are listed in Table S1. The transformed cells were grown into a large-scale culture and induced with 0.1mM IPTG for 3 h at 37°C. The cells were collected at 4,000 rpm for 20 min and the cell pellet was resuspended in lysis buffer (50 mM Tris-HCl pH 8.0, 1mM EDTA, 25% sucrose, 0.5mM PMSF, 1.2 mg/mL lysozyme). After 30 min incubation on ice, 6mM of $MgCl_2$, 0.6mM of $MnCl_2$, and 0.03 mM of DNase I were added, then incubated on ice for another 30 min. Detergent buffer (0.2 M NaCl, 1% deoxycholic acid, 1% Nonidet P-40, 20mM Tris-HCl pH 7.4, 2mM EDTA) was added and the suspension was centrifuged at 5,000 g, 4°C for 10 min. The supernatant was removed, the cell pellet was resuspended in Tx-EDTA buffer (0.5% Triton X-100, 1 mM EDTA), and the suspension was centrifuged again at 5,000 g, 4°C for 10 min. The steps of resuspension in Tx-EDTA buffer and spinning down of the cell pellet were repeated 4–5 times until a tight inclusion body pellet was obtained. The inclusion body was resuspended in equilibration buffer (20 mM sodium phosphate, 300 mM sodium chloride, 10 mM imidazole, 6.5 M urea), and the residual detergent was removed by using centricon and spinning down at 7,500 g, 4°C for 30 min. Subsequently, the inclusion bodies of keratins 8 and 18 were mixed in equal amounts and affinity purified using HisPur Ni-NTA Resin (ThermoScientific) according to the manufacturer's protocol with the addition of urea in buffers. Equilibration buffer (20 mM sodium phosphate, 300 mM sodium chloride, 10mM imidazole, 6.5 M urea), wash buffer (20 mM sodium phosphate, 300 mM sodium chloride, 25 mM imidazole, 6.5 M urea), and

elution buffer (20 mM sodium phosphate, 300 mM sodium chloride, 250 mM imidazole, 6.5 M urea) with pH of 7.4 were used.

GFP-tagged LIM proteins purification—GFP-tagged LIM proteins were inserted into pET-28 vector, flanked by sfGFP and StrepII tags, and each expressed in Rosetta2(DE3) (Novagen). The primers used are listed in Table S1. The transformed cells were grown into a large-scale culture and induced with 0.1 mM IPTG for 16 h at 16°C. Bacterial cells were harvested by centrifugation, lysed in lysis buffer (100 mM Tris-HCl pH 8.0, 150 mM sodium chloride, 1 mM EDTA, 1 mM dithiothreitol, 1 mM ATP, 2 mM magnesium sulfate, 1% Triton X-100, 0.1 mM PMSF or oComplete Mini tablets, 4 mg/mL lysozyme), and sonicated to shear chromosomal DNA until suspension became homogeneous. Proteins were collected in the supernatant after centrifugation at 10,000 rpm for 20 min at 4°C and affinity purified using Strep-Tactin XT Resin (IBA Lifesciences) according to the manufacturer's protocol with some modifications in buffer compositions. Wash I buffer (100 mM Tris-HCl pH 8.0, 150 mM sodium chloride, 1 mM EDTA, 1 mM dithiothreitol, 1 mM ATP, 2.5 mM magnesium sulfate, 0.1 mM PMSF), Wash II buffer (100 mM Tris-HCl pH 8.0, 150 mM sodium chloride, 1 mM EDTA), and elution buffer (100 mM Tris-HCl pH 8.0, 150mM sodium chloride, 1mM EDTA, 100mM biotin) were used. Final protein concentrations were measured using Bradford assay (Bio-Rad), and the purified proteins were aliquoted and frozen in dry ice ethanol bath and stored at −80°C.

Microscopy system and softwares—Cells were imaged using a Zeiss AxioObserver equipped with a Yokogawa CSU-10 spinning disk confocal system, 10x, 40x; and 63x objectives, 488- and 561-nm solid-state lasers, an ASI motorized microscope stage and a Photometrics CoolSNAP HQ2 camera. The microscope system was controlled by Slidebook software (Intelligent Imaging Innovations). For live-cell imaging, the temperature was set to 37°C by a custom microscope heating chamber and the media was supplemented with 25 mM HEPES (Invitrogen), otherwise the microscope system was kept at room temperature. The microscope system is also equipped with a Micropoint laser ablation system (Photonics Instrument) that consists of a fiber optically pumped dye laser and a computer-controlled beam position and intensity. This system was used for fluorescence recovery analysis described below. All images were analyzed using ImageJ and Microsoft Excel, and graphed using PlotsofData,[49] KaleidaGraph, or GraphPad Prism 10. Image analysis specific to the experiments are described below.

Microneedle cell stretching analysis—Custom drawn needles were fabricated from a glass rod (OD = 1 mm) using a Sutter P-97 Micropipette puller with following parameters HEAT = 950, VEL = 50, TIME = 150. To maximize the microneedle's contact with adherent cells, the tip of microneedle was bent with a mini torch to touch the dorsal side of cells at a shallow angle, while the rest of the microneedle was carefully bent at a 90-degree angle in opposite directions to clear the sidewall of a p35 glass bottom dish (CellVis). The microneedle was attached to a 3D micromanipulator (Physik Instrumente) controlled with a gaming joystick and a custom-written software.

The cells were plated onto collagen-coated glass bottom dish for at least one day to ensure the adhesion between cells as well as to the substrate. In most experiments, cells were plated

at 60–100% cell confluency to ensure that formation of mature cell-cell junctions. For the co-localization analysis of LIM proteins and the actin cytoskeleton, cells were plated at less than 50% cell confluency to promote the formation of more visible actin stress fibers. Then, the culture dish was transferred to the microscope preheated at 37°C. Initially, the microneedle was placed into the dish and gradually lowered to the cell surface using a 10x objective, then switched to a 40x objective for subcellular imaging of protein dynamics.

The microneedle was carefully placed on neighboring sacrificial cells, often at the nucleus, then gently moved away from the cells of interest (denoted by yellow arrows in the figures) to transmit mechanical strain to the target cells across cell-cell contacts. Movement of microneedle in all three dimensions was manually controlled to ensure that the microneedle maintained its contact with the sacrificial/neighboring cells and the consistent stretch rate of target cells. In rare occasions, the cells became out-of-focus due to temperature shifting or microneedle lifting the cells, then the optical focus was manually adjusted to ensure the best fiber detection. Note that none of the cells analyzed came in direct contact with the microneedle. Time-lapse images were taken with a 10 s time interval.

For the inhibitor treatment, the imaging media was replaced with the media with an appropriate inhibitor prior to the placement on the microscope (EGTA) or during the image acquisition (cytochalasin D and thapsigargin). When the media was replaced on the microscope stage, we gently aspirated the media using a pasteur pipet connected to a house vacuum, and the replacement media was added, and this procedure was repeated at least once to minimize the dilution of the inhibitors.

The quantification of LIM protein accumulation along fibrous structures was performed as described below using ImageJ software. The images were exported as 16 bit TIF files from Slidebook. Since the intensity of LIM protein accumulation along the fibers often exceeded the cytoplasmic intensity, the thresholding based on fluorescence intensity was used to define the areas of LIM protein accumulation. To define the fiber area, the post-stretch image was selected based on the highest protein accumulation from the time-lapse images. The outlines of pre- and post-stretch cells were created manually so that fiber detection was limited to within the cell area. Some LIM proteins localized to the nucleus in the absence of force, but their nuclear signal was excluded from the analysis by manually defining the nuclear boundary, which was combined with cell outline using XOR function in ImageJ ROI manager.

The Background Subtraction command with a rolling ball radius of 5 pixels in ImageJ was used to minimize the background intensity fluctuations and non-fibrous cytoplasmic signals. The difference in the thresholded areas (fiber area) from pre-stretch and post-stretch images was used as a proxy for the extent of protein accumulation along the force-bearing fibers. Based on the post-stretch cell image, the threshold value was defined manually to maximize the selection of force-induced accumulation, while minimizing noise and background fluorescence. Then, the identical threshold value was applied to the pre-stretch image to define the prestretch fiber accumulation (e.g., proteins already bound to actin filaments prior to stretch or focal adhesions). This approach ensured that a uniform standard was applied to both images to minimize any potential bias. Unlike fibroblasts, MDCK cells

do not have extensive actin stress fibers or large focal adhesions, especially in confluent cell monolayer, thus thresholded areas in pre-stretch images were often minimal. The individual thresholded areas were counted and measured using “Analyze Particles” function in ImageJ with the minimum particle size of 5 pixels, then combined to create one single selection of all detected regions. A custom macro in ImageJ was written to run the series of commands described above, and the measured parameters were displayed in ResultsTable then copied to Excel for further analysis. In Excel, the difference in thresholded areas from pre-stretch and post-stretch images were calculated and normalized to the initial cell area – this value is plotted as GFP accumulation in the figures.

For the line scan analysis, profile lines were placed manually where both LIM protein accumulation and cytoskeletal marker (i.e., zyxin, cten or keratin) accumulation are clearly discernible and the profile line intersects both fibers. The co-localization of LIM proteins and the cytoskeletal markers was determined by the measurements of the intensity peaks as well as the relative position of the profile lines within the cell.

***In vitro* stretch assay—**The recombinant His-tagged keratin 8 and keratin 18 were assembled into filaments via serial dialysis[50]: (1) 8 M urea, 25mMTris-HCl, 10 mM β-mercaptoethanol, pH 7.4 for 4 h at 4°C (2) 2M urea for >2 h at 4°C, (3) 5 mM Tris-HCl, 5 mM β-mercaptoethanol, pH 7.4 overnight at room temperature. Assembled filaments were adsorbed onto a clean coverslip, blocked with 1 mg/mL BSA in PBS, and visualized using fluorescently labeled anti-His antibody (Invitrogen). Similar to the microneedle-based cell stretch analysis (see detailed protocol above), the recombinant keratin filaments were stretched using a microneedle under the control of a micro-manipulator. After successful application of strain onto the filaments, purified GFP-tagged proteins, pre-diluted at a concentration of 1 mM in PBS containing 1 mg/mL BSA and 1 mM Zn^{2+}, were added and incubated for 5 min.

To quantify the accumulation of GFP-tagged LIM proteins along the force-bearing keratin filament bundles, the Segmented Line tool with Fit Spline function in ImageJ was used to manually trace stretched versus unstretched regions along the filament bundles. The mean intensities of GFP- and His-fluorescence along these ROIs, as well as the filament lengths pre- and post-stretch, were measured in ImageJ and their ratios (GFP-tagged proteins/His-K8) were analyzed in Microsoft Excel. A custom macro in ImageJ was written to run the series of commands described above. The percent strain was determined by the equation below, where length refers to the segment of keratin bundles being stretched. Unstretched segments (Control in Figure 3E) were assigned a strain value of 0 as there was no change from the initial length to the final length.

$$\%strain = \frac{final\ length - initial\ length}{initial\ length} * 100$$

Fluorescence recovery after photo bleaching (FRAP) analysis—To monitor the turnover of LIM proteins in the surface of keratin fibers both *in vitro* and in live cells, the GFP-tagged LIM proteins were either purified and added to pre-stretch fibers *in vitro* or

transfected in live cells. Using a Micropoint photoablation system (Photonics Instrument) and Coumarin 440 dye, the laser position and power were carefully calibrated to ensure that diffraction limited spots were photobleached without damaging protein samples or the cells. The laser pulses (1–5 pluses) were fired based on a mouse click on the captured GFP image in Slidebook software. Upon stretching of the purified keratin fibers or live cells (as described above), GFP-LIM proteins accumulated along keratin fibers both *in vitro* and in live cells, then the laser pulses were aimed and fired at the GFP accumulation which created a photobleached spot, and the fluorescence intensity was monitored over time (5 and 10 s interval for *in vitro* analysis and live cells, respectively). Time-lapse images were exported as a 16 bit TIF files and analyzed in ImageJ.

In ImageJ, the FRAP spot was defined as a circular selection, and another selection away from FRAP spot was also defined to track background photobleaching from image acquisition. The intensity was then measured for each frame over time, and copied to an Excel file for further analysis. First, the fluorescence intensity values were normalized to the fluorescence signal away from FRAP regions to correct for photobleaching from image acquisition. Second, the fluorescence intensity was normalized using pre-photobleach intensity ($F0$) and immediately after photobleaching ($F_{\min}$) using the following formula: $(F(t) - F_{min})/(F0 - F_{min})$. The initial slope (k, Figure 4E) of fluorescence recovery was calculated using a curve fitting of exponential function $\left(1 - e^{-kt}\right)$, while the mobile fraction (Figure 4F) was calculated based on the recovery at 4 min where most recovery profiles reached a plateau value.

QUANTIFICATION AND STATISTICAL ANALYSIS

To characterize the fibrous accumulation of LIMK1 mutants and LMO1 truncations (Figure 2), as well as to compare the average intensity ratios of LIM protein accumulation along force-bearing keratin fibers *in vitro* (Figure 3), Dunnett's test was employed. For the comparison of the initial rate k and mobile fraction of fluorescence recovery of LIMK1-S337E and LMO1-LIM *in vitro* and in live cells, one-way ANOVA test with a confidence interval of 95% was employed. Statistical significance was set at $p \leq 0.05$. Asterisks indicate $*p < 0.05$; $**p < 0.01$; $***p < 0.001$; $****p < 0.0001$; n.s. (not significant), $p > 0.05$.

Data representation and statistical analysis were performed in Microsoft Excel, Kaleidagraph, PlotsOfData, and GraphPad Prism 10.

Supplementary Material

Refer to Web version on PubMed Central for supplementary material.

ACKNOWLEDGMENTS

This work was supported by NSF 1562095 (to S.Y., REU supplement to J.S.C.), UC CRCC C21CR2138 (to S.Y., diversity supplement to T.W.L.), NIH R01 GM148706 (to S.Y.), and UC Davis Provost's Undergraduate Fellowships (to J.S.C., T.W.L., K.X.Z., and S.R.F.). J.S.C. is a recipient of the Beckman Scholars Award.

REFERENCES

1. Kadrmas JL, and Beckerle MC (2004). The LIM domain: from the cytoskeleton to the nucleus. Nat. Rev. Mol. Cell Biol 5, 920–931. 10.1038/nrm1499. [PubMed: 15520811]
2. Koch BJ, Ryan JF, and Baxevanis AD (2012). The diversification of the LIM superclass at the base of the metazoa increased subcellular complexity and promoted multicellular specialization. PLoS One 7, e33261. 10.1371/journal.pone.0033261. [PubMed: 22438907]
3. Kuo JC, Han X, Hsiao CT, Yates JR 3rd, and Waterman CM (2011). Analysis of the myosin-II-responsive focal adhesion proteome reveals a role for beta-Pix in negative regulation of focal adhesion maturation. Nat. Cell Biol 13, 383–393. 10.1038/ncb2216. [PubMed: 21423176]
4. Schiller HB, Friedel CC, Boulegue C, and Fässler R (2011). Quantitative proteomics of the integrin adhesome show a myosin II-dependent recruitment of LIM domain proteins. EMBO Rep. 12, 259–266. 10.1038/embor.2011.5. [PubMed: 21311561]
5. Colombelli J, Besser A, Kress H, Reynaud EG, Girard P, Caussinus E, Haselmann U, Small JV, Schwarz US, and Stelzer EHK (2009). Mechanosensing in actin stress fibers revealed by a close correlation between force and protein localization. J. Cell Sci 122, 1665–1679. 10.1242/jcs.042986. [PubMed: 19401336]
6. Watanabe-Nakayama T, Saito M, Machida S, Kishimoto K, Afrin R, and Ikai A (2013). Requirement of LIM domains for the transient accumulation of paxillin at damaged stress fibres. Biol. Open 2, 667–674. 10.1242/bio.20134531. [PubMed: 23862014]
7. Cheah JS, Jacobs KA, Lai TW, Caballelo R, Yee JL, Ueda S, Heinrich V, and Yamada S (2021). Spatial proximity of proteins surrounding zyxin under force-bearing conditions. Mol. Biol. Cell 32, 1221–1228. 10.1091/mbc.E19-10-0568. [PubMed: 33909446]
8. Yoshigi M, Hoffman LM, Jensen CC, Yost HJ, and Beckerle MC (2005). Mechanical force mobilizes zyxin from focal adhesions to actin filaments and regulates cytoskeletal reinforcement. J. Cell Biol 171, 209–215. 10.1083/jcb.200505018. [PubMed: 16247023]
9. Hoffman LM, Jensen CC, Chaturvedi A, Yoshigi M, and Beckerle MC (2012). Stretch-induced actin remodeling requires targeting of zyxin to stress fibers and recruitment of actin regulators. Mol. Biol. Cell 23, 1846–1859. 10.1091/mbc.E11-12-1057. [PubMed: 22456508]
10. Hirata H,Tatsumi H and Sokabe M (2008). Mechanical forces facilitate actin polymerization at focal adhesions in a zyxin-dependent manner. J. Cell Sci 121,2795–2804. [PubMed: 18682496]
11. Sun X, Phua DYZ, Axiotakis L Jr., Smith MA, Blankman E, Gong R, Cail RC, Espinosa de Los Reyes S, Beckerle MC, Waterman CM, and Alushin GM (2020). Mechanosensing through Direct Binding of Tensed F-Actin by LIM Domains. Dev. Cell 55, 468–482.e7. 10.1016/j.devcel.2020.09.022. [PubMed: 33058779]
12. Dutta S, Mana-Capelli S, Paramasivam M, Dasgupta I, Cirka H, Billiar K, and McCollum D (2018). TRIP6 inhibits Hippo signaling in response to tension at adherens junctions. EMBO Rep. 19, 337–350. 10.15252/embr.201744777. [PubMed: 29222344]
13. Smith MA, Blankman E, Deakin NO, Hoffman LM, Jensen CC, Turner CE, and Beckerle MC (2013). LIM Domains Target Actin Regulators Paxillin and Zyxin to Sites of Stress Fiber Strain. PLoS One 8, e69378. 10.1371/journal.pone.0069378. [PubMed: 23990882]
14. Smith MA, Blankman E, Gardel ML, Luettjohann L, Waterman CM, and Beckerle MC (2010). A zyxin-mediated mechanism for actin stress fiber maintenance and repair. Dev. Cell 19, 365–376. 10.1016/j.devcel.2010.08.008. [PubMed: 20833360]
15. Oakes PW, Wagner E, Brand CA, Probst D, Linke M, Schwarz US, Glotzer M, and Gardel ML (2017). Optogenetic control of RhoA reveals zyxin-mediated elasticity of stress fibres. Nat. Commun 8, 15817. 10.1038/ncomms15817. [PubMed: 28604737]
16. Winkelman JD, Anderson CA, Suarez C, Kovar DR, and Gardel ML (2020). Evolutionarily diverse LIM domain-containing proteins bind stressed actin filaments through a conserved mechanism. Proc. Natl. Acad. Sci. USA 117, 25532–25542. 10.1073/pnas.2004656117. [PubMed: 32989126]
17. Sala S, and Oakes PW (2021). Stress fiber strain recognition by the LIM protein testin is cryptic and mediated by RhoA. Mol. Biol. Cell 32, 1758–1771. 10.1091/mbc.E21-03-0156. [PubMed: 34038160]

18. Uemura A, Nguyen TN, Steele AN, and Yamada S (2011). The LIM domain of zyxin is sufficient for force-induced accumulation of zyxin during cell migration. Biophys. J 101, 1069–1075. 10.1016/j.bpj.2011.08.001. [PubMed: 21889443]
19. Lele TP, Pendse J, Kumar S, Salanga M, Karavitis J, and Ingber DE (2006). Mechanical forces alter zyxin unbinding kinetics within focal adhesions of living cells. J. Cell. Physiol 207, 187–194. 10.1002/jcp.20550. [PubMed: 16288479]
20. Zhang JS, Gong A, and Young CYF (2007). ZNF185, an actin-cytoskeleton-associated growth inhibitory LIM protein in prostate cancer. Oncogene 26, 111–122. 10.1038/sj.onc.1209769. [PubMed: 16799630]
21. Maul RS, Song Y, Amann KJ, Gerbin SC, Pollard TD, and Chang DD (2003). EPLIN regulates actin dynamics by cross-linking and stabilizing filaments. J. Cell Biol 160, 399–407. 10.1083/jcb.200212057. [PubMed: 12566430]
22. Schreiber V, Moog-Lutz C, Régnier CH, Chenard MP, Boeuf H, Vonesch JL, Tomasetto C, and Rio MC (1998). Lasp-1, a novel type of actin-binding protein accumulating in cell membrane extensions. Mol. Med 4, 675–687. [PubMed: 9848085]
23. Bauer K, Kratzer M, Otte M, de Quintana KL, Hagmann J, Arnold GJ, Eckerskorn C, Lottspeich F, and Siess W (2000). Human CLP36, a PDZ-domain and LIM-domain protein, binds to alpha-actinin-1 and associates with actin filaments and stress fibers in activated platelets and endothelial cells. Blood 96, 4236–4245. [PubMed: 11110697]
24. Vallenius T, Luukko K, and Mäkelä TP (2000). CLP-36 PDZ-LIM protein associates with nonmuscle alpha-actinin-1 and alpha-actinin-4. J. Biol. Chem 275, 11100–11105. 10.1074/jbc.275.15.11100. [PubMed: 10753915]
25. Yang N, Higuchi O, Ohashi K, Nagata K, Wada A, Kangawa K, Nishida E, and Mizuno K (1998). Cofilin phosphorylation by LIM-kinase 1 and its role in Rac-mediated actin reorganization. Nature 393, 809–812. 10.1038/31735. [PubMed: 9655398]
26. Cheah JS, Jacobs KA, Heinrich V, Lo SH, and Yamada S (2019). Force-induced recruitment of cten along keratin network in epithelial cells. Proc. Natl. Acad. Sci. USA 116, 19799–19801. 10.1073/pnas.1911865116. [PubMed: 31527270]
27. Nagata K, Ohashi K, Yang N, and Mizuno K (1999). The N-terminal LIM domain negatively regulates the kinase activity of LIM-kinase 1. Biochem. J 343, 99–105. [PubMed: 10493917]
28. Hiraoka J, Okano I, Higuchi O, Yang N, and Mizuno K (1996). Self-association of LIM-kinase 1 mediated by the interaction between an N-terminal LIM domain and a C-terminal kinase domain. FEBS Lett. 399, 117–121. 10.1016/s0014-5793(96)01303-8. [PubMed: 8980133]
29. Yang N, and Mizuno K (1999). Nuclear export of LIM-kinase 1, mediated by two leucine-rich nuclear-export signals within the PDZ domain. Biochem. J 338, 793–798. [PubMed: 10051454]
30. Kobayashi M, Nishita M, Mishima T, Ohashi K, and Mizuno K (2006). MAPKAPK-2-mediated LIM-kinase activation is critical for VEGF-induced actin remodeling and cell migration. EMBO J. 25, 713–726. 10.1038/sj.emboj.7600973. [PubMed: 16456544]
31. Daub H, Olsen JV, Bairlein M, Gnad F, Oppermann FS, Körner R, Greff Z, Kéri G, Stemmann O, and Mann M (2008). Kinase-selective enrichment enables quantitative phosphoproteomics of the kinome across the cell cycle. Mol. Cell 31, 438–448. 10.1016/j.molcel.2008.07.007. [PubMed: 18691976]
32. Sawant MS, and Leube RE (2017). Consequences of Keratin Phosphorylation for Cytoskeletal Organization and Epithelial Functions. Int. Rev. Cell Mol. Biol 330, 171–225. 10.1016/bs.ircmb.2016.09.005. [PubMed: 28215532]
33. Deane JE, Ryan DP, Sunde M, Maher MJ, Guss JM, Visvader JE, and Matthews JM (2004). Tandem LIM domains provide synergistic binding in the LMO4:Ldb1 complex. EMBO J. 23, 3589–3598. 10.1038/sj.emboj.7600376. [PubMed: 15343268]
34. Matthews JM, Lester K, Joseph S, and Curtis DJ (2013). LIM-domain-only proteins in cancer. Nat. Rev. Cancer 13, 111–122. 10.1038/nrc3418. [PubMed: 23303138]
35. Moch M, Herberich G, Aach T, Leube RE, and Windoffer R (2013). Measuring the regulation of keratin filament network dynamics. Proc. Natl. Acad. Sci. USA 110, 10664–10669. 10.1073/pnas.1306020110. [PubMed: 23757496]

36. Sivaramakrishnan S, Schneider JL, Sitikov A, Goldman RD, and Ridge KM (2009). Shear stress induced reorganization of the keratin intermediate filament network requires phosphorylation by protein kinase C zeta. Mol. Biol. Cell 20, 2755–2765. 10.1091/mbc.e08-10-1028. [PubMed: 19357195]
37. Yoon KH, Yoon M, Moir RD, Khuon S, Flitney FW, and Goldman RD (2001). Insights into the dynamic properties of keratin intermediate filaments in living epithelial cells. J. Cell Biol 153, 503–516. 10.1083/jcb.153.3.503. [PubMed: 11331302]
38. Lappalainen P, Kotila T, Jégou A, and Romet-Lemonne G (2022). Biochemical and mechanical regulation of actin dynamics. Nat. Rev. Mol. Cell Biol 23, 836–852. 10.1038/s41580-022-00508-4. [PubMed: 35918536]
39. Harris AR, Jreij P, and Fletcher DA (2018). Mechanotransduction by the Actin Cytoskeleton: Converting Mechanical Stimuli into Biochemical Signals. Annu. Rev. Biophys 47, 617–631. 10.1146/annurev-biophys-070816-033547.
40. Sun X, and Alushin GM (2023). Cellular force-sensing through actin filaments. FEBS J. 290, 2576–2589. 10.1111/febs.16568. [PubMed: 35778931]
41. Block J, Witt H, Candelli A, Danes JC, Peterman EJG, Wuite GJL, Janshoff A, and Köster S (2018). Viscoelastic properties of vimentin originate from nonequilibrium conformational changes. Sci. Adv 4, eaat1161. 10.1126/sciadv.aat1161. [PubMed: 29928696]
42. Fleissner F, Kumar S, Klein N, Wirth D, Dhiman R, Schneider D, Bonn M, and Parekh SH (2020). Tension Causes Unfolding of Intracellular Vimentin Intermediate Filaments. Adv. Biosyst 4, e2000111. 10.1002/adbi.202000111. [PubMed: 33135378]
43. Qin Z, Kreplak L, and Buehler MJ (2009). Hierarchical structure controls nanomechanical properties of vimentin intermediate filaments. PLoS One 4, e7294. 10.1371/journal.pone.0007294. [PubMed: 19806221]
44. Nunes Vicente F, Lelek M, Tinevez JY, Tran QD, Pehau-Arnaudet G, Zimmer C, Etienne-Manneville S, Giannone G, and Leduc C (2022). Molecular organization and mechanics of single vimentin filaments revealed by super-resolution imaging. Sci. Adv 8, eabm2696. 10.1126/sciadv.abm2696. [PubMed: 35213220]
45. Hu J, Li Y, Hao Y, Zheng T, Gupta SK, Parada GA, Wu H, Lin S, Wang S, Zhao X, et al. (2019). High stretchability, strength, and toughness of living cells enabled by hyperelastic vimentin intermediate filaments. Proc. Natl. Acad. Sci. USA 116, 17175–17180. 10.1073/pnas.1903890116. [PubMed: 31409716]
46. Fudge D, Russell D, Beriault D, Moore W, Lane EB, and Vogl AW (2008). The intermediate filament network in cultured human keratinocytes is remarkably extensible and resilient. PLoS One 3, e2327. 10.1371/journal.pone.0002327. [PubMed: 18523546]
47. Fujiwara S, Ohashi K, Mashiko T, Kondo H, and Mizuno K (2016). Interplay between Solo and keratin filaments is crucial for mechanical force-induced stress fiber reinforcement. Mol. Biol. Cell 27, 954–66. 10.1091/mbc.E15-06-0417. [PubMed: 26823019]
48. Janmey PA, Euteneuer U, Traub P, and Schliwa M (1991). Viscoelastic properties of vimentin compared with other filamentous biopolymer networks. J. Cell Biol 113, 155–160. 10.1083/jcb.113.1.155. [PubMed: 2007620]
49. Postma M, and Goedhart J (2019). PlotsOfData-A web app for visualizing data together with their summaries. PLoS Biol. 17, e3000202. 10.1371/journal.pbio.3000202. [PubMed: 30917112]
50. Yamada S, Wirtz D, and Coulombe PA (2002). Pairwise assembly determines the intrinsic potential for self-organization and mechanical properties of keratin filaments. Mol. Biol. Cell 13, 382–391. 10.1091/mbc.01-10-0522. [PubMed: 11809846]

Highlights

- LIMK1 and LMO1 proteins selectively and directly bind to force-bearing keratin filaments
- This unique recruitment is regulated by the sequences outside the LIM domains
- The dynamic nature of LIMK1 and LMO1 binding suggests their role in downstream signaling
- The keratin network may serve as a signaling hub for mechano-transduction

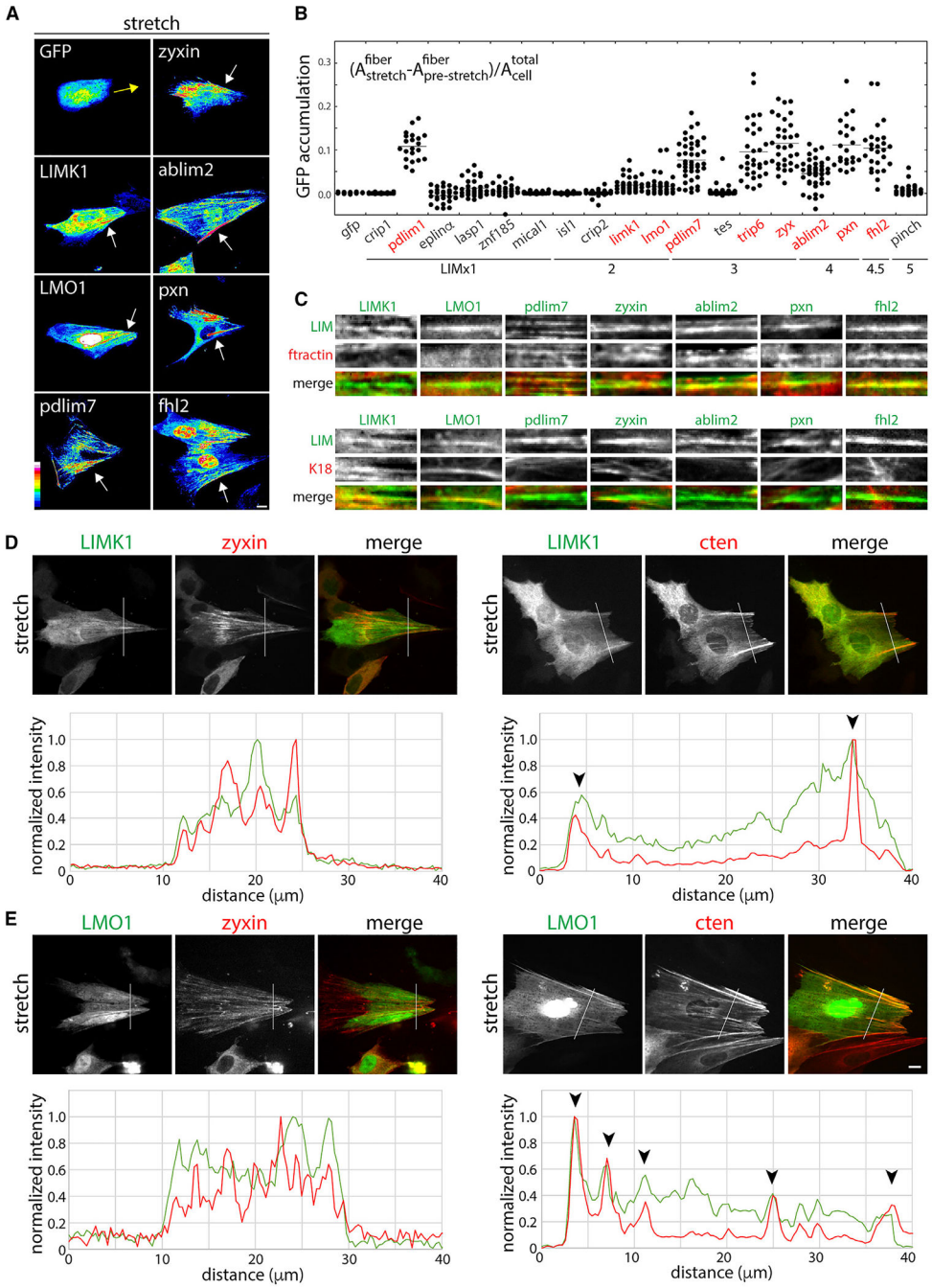

Figure 1. Force-induced accumulation of LIMK1 and LMO1 along keratin fibers

(A) Accumulation of the full-length LIMK1, LMO1, pdlim7, zyxin, ablim2, pxn, and fhl2 along fibers upon stretch. Yellow arrow and white arrows denote the stretch direction and stretch-induced LIM protein accumulation, respectively. The scale bar (10 μm) applies to all images.

(B) Quantification of the full-length GFP and GFP-tagged LIM protein accumulation.

(C) Co-localization between LIMK1, LMO1, pdlim7, zyxin, ablim2, pxn, and fhl2 with F-tractin and keratin 18 fibers in stretched cells.

(D and E) Force-induced accumulation of LIMK1 proteins (D) and LMO1 proteins (E) relative to zyxin and cten. Scale bar, 10 μm.

See also Figures S1 and S2 and Videos S1, S2, and S3.

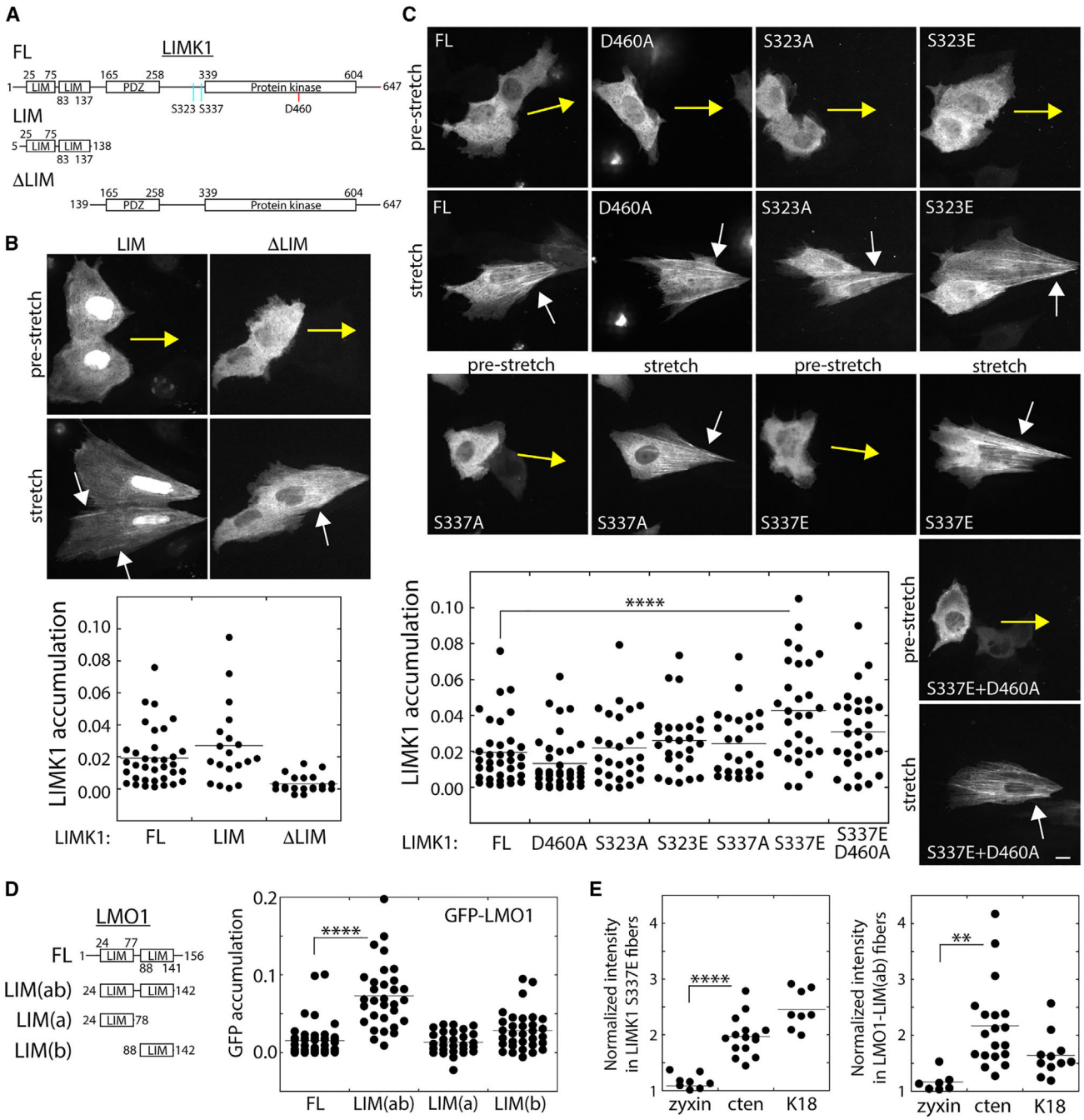

Figure 2. Force-induced recruitment of LIMK1 and LMO depends on their LIM domains and is along keratin fibers

(A) Schematic of LIMK1 truncation mutants and the location of point mutations.

(B) Comparison of LIMK1-LIM and ΔLIM force sensitivity.

(C) Force-induced accumulation of the LIMK1 kinase-dead mutant (D460A) and phospho-mutants (S323 and S337). Yellow arrows indicate the direction of microneedle movement, and white arrows indicate the location of force-induced accumulation. The scale bar (10 μm) applies to all images.

(D) Comparison of the force sensitivities of LMO1 truncation mutants containing two LIM(ab) domains or single LIM(a or b) domains.
(E) Quantification of zyxin, cten, and keratin 18 intensity in LIMK1-positive fibers and LMO1-LIM(ab)-positive fibers. ** and **** represent $p < 0.01$ and $p < 0.0001$, respectively. See also Figures S1 and S3.

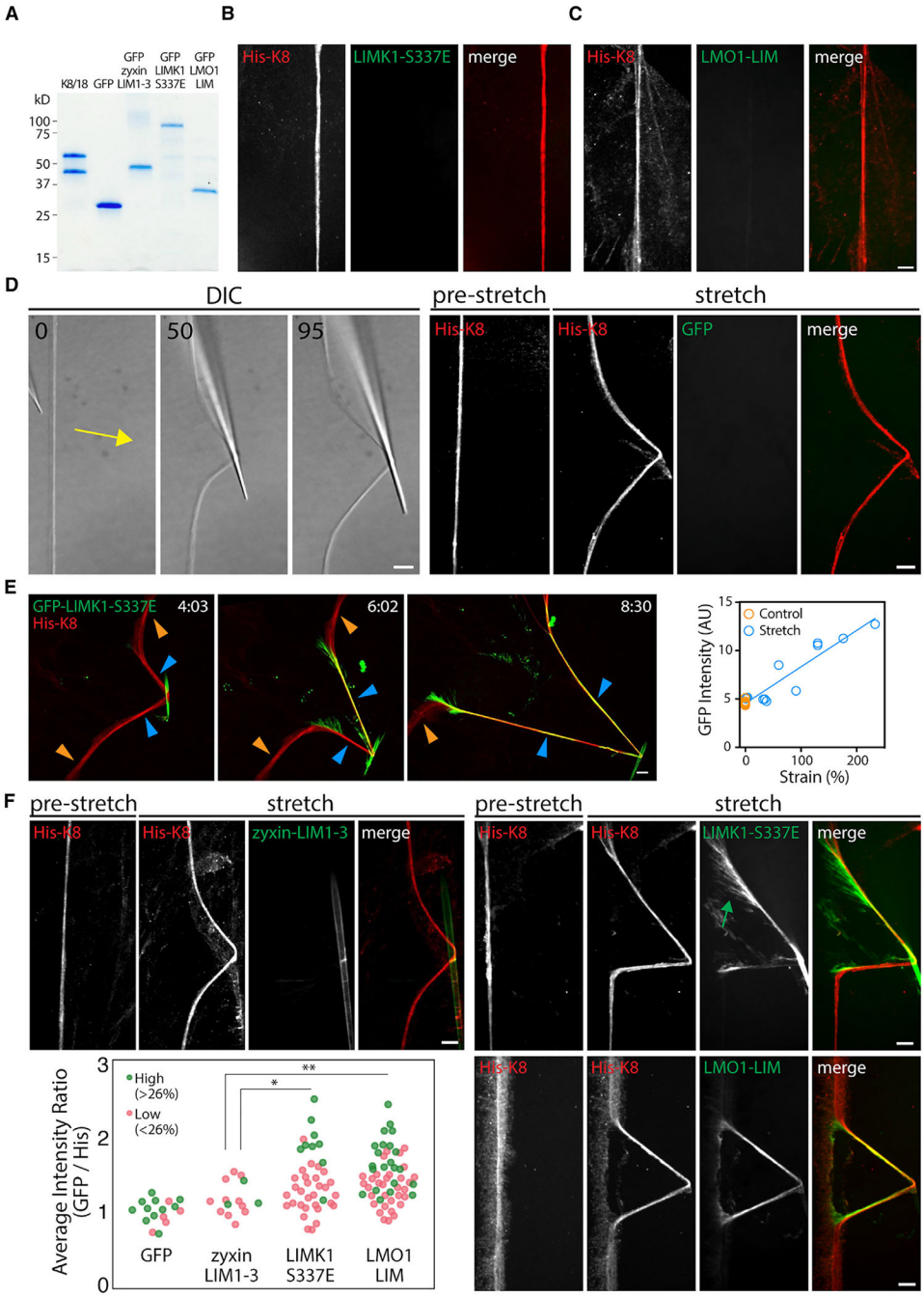

Figure 3. *In vitro* reconstitution of the keratin network under strain

(A) Coomassie blue-stained SDS-PAGE gel of purified K8/18, GFP, and GFP-tagged LIM proteins.

(B and C) LIM protein interactions with surface-bound keratin filaments. Shown are fluorescence signals from keratin 8 fibers (anti-His antibody, red) and GFP-LIMK1-S337E (green) (B), and GFP-LMO1-LIM (C) in the absence of strain.

(D) Bright-field and fluorescence images of surface-bound keratin fibers being stretched using a microneedle. A yellow arrow denotes the stretch direction. Time is in seconds.

Fluorescence signals from keratin 8 fibers (anti-His antibody, red) and GFP alone as a control (green).

(E) Fluorescence time-lapse images of GFP-LIMK1-S337E accumulation at increasing strain and analysis of strain dependence. Orange and blue arrowheads indicate control (unstretched) and stretch (strained) regions of the keratin bundle, respectively. See also Video S4.

(F) Fluorescence labeling of keratin 8 fibers (anti-His antibody, red), GFP-zyxin-LIM1-3 (green), GFP-LIMK1-S337E (green), and GFP-LMO1-LIM (green). Intensity ratio of GFP-tagged proteins to His-tagged keratin 8 under low (<26%) and high (>26%) strain. LIMK1-S337E and LMO1-LIM selectively accumulated along strained keratin filaments while zyxin did not (*and ** represent $p < 0.05$ and $p < 0.01$, respectively. $p < 0.001$ for GFP and LIMK1-S337E and $p < 0.00001$ for GFP and LMO1-LIM). A green arrow indicates GFP-LIMK1-S337E accumulation along finer keratin fibers; see also Figure S4 for high-contrast images and alternative examples. Time is in min:seconds. Scale bars, 10 μm.

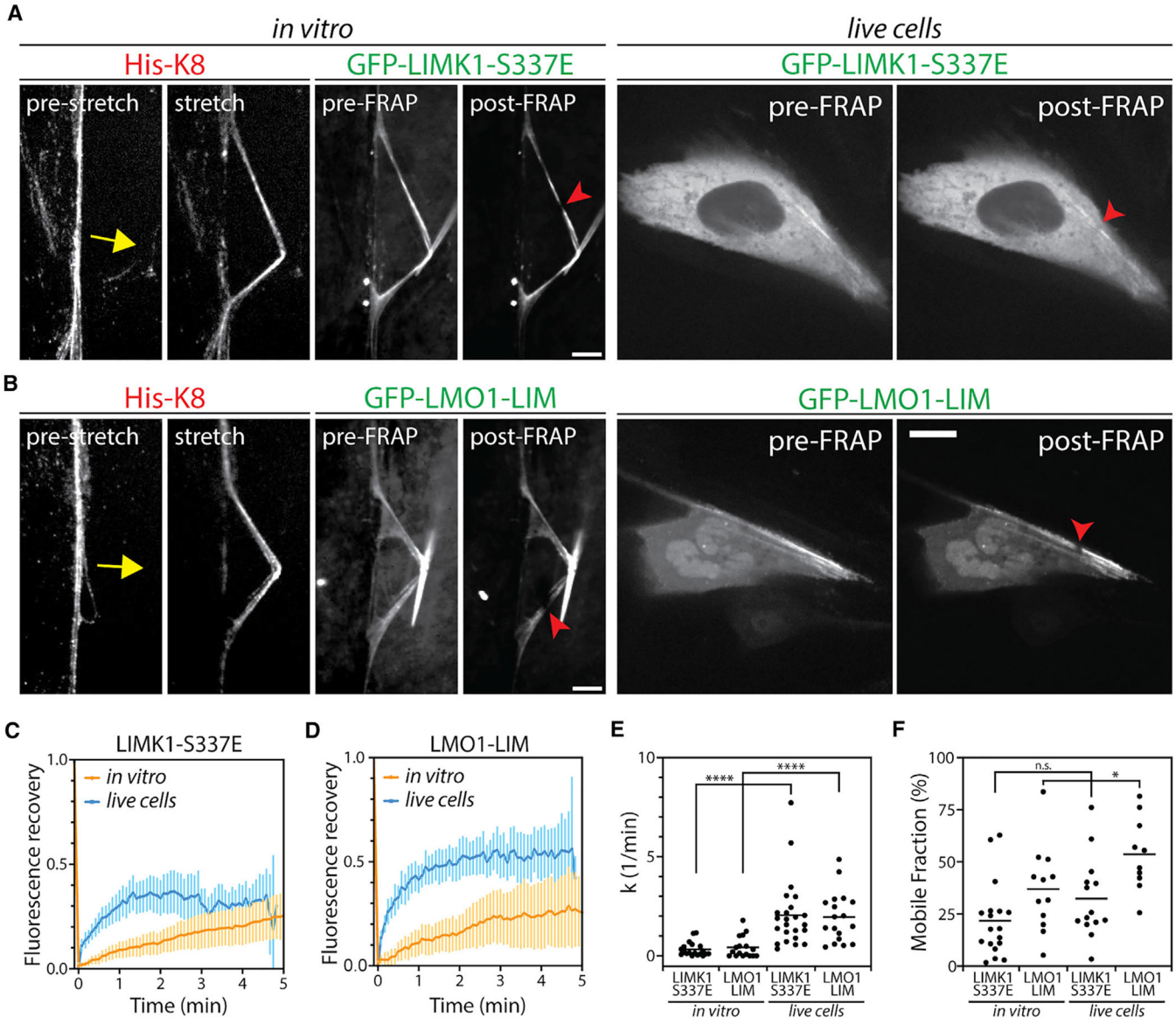

Figure 4. FRAP analysis of LIMK1 and LMO1 dynamics

(A and B) Fluorescence labeling of keratin 8 fibers (anti-His antibody, red) before and after stretching and pre- and post-FRAP images of GFP-LIMK1-S337E (green) (A) and GFP-LMO1-LIM (green) (B) *in vitro* and in live cells. Yellow arrows and red arrowheads indicate stretching direction and FRAP locations, respectively. Scale bars, 10 ɔm.

(C and D) Averaged *in vitro* and live-cell FRAP data of GFP-LIMK1-S337E (C) and GFP-LMO1-LIM (D) over time (minutes), with ±95% confidence interval.

(E and F) Quantification of the initial rate k (E) and mobile fraction (F) of fluorescence recovery at 4 min. n.s., *, and **** represent $p > 0.05$, $p < 0.05$, and $p < 0.0001$, respectively.

KEY RESOURCES TABLE

REAGENT or RESOURCE	SOURCE	IDENTIFIER
Antibodies		
Anti-HIS antibody, Alexa Fluor 555	Invitrogen	Cat# MA1-21315-A555; RRID:AB_2610646
Anti-keratin 8 antibody [EP1628Y]	Abcam	ab53280; RRID:AB_869901
Anti-alpha-tubulin antibody DM1A	Cell signaling technology	3873; RRID:AB_1904178
Anti-rabbit IgG HRP conjugate	Bio-Rad	170–6515; RRID:AB_11125142
Anti-mouse IgG HRP conjugate	Bio-Rad	170–6516; RRID:AB_11125547
Bacterial and virus strains		
Lemo21 (DE3) Competent E. Coli	NEB	Cat# C2528J
Rosetta 2 (DE3) Competent Cells	Novagen	Cat# 71397
NEB® 5-alpha Competent E. coli (High Efficiency)	NEB	Cat# C2987I
Chemicals, peptides, and recombinant proteins		
HEPES	Sigma	Cat# H3375
D-Biotin	Chem-Impex	Cat# 00033
Lysozyme	ThermoFisher	Cat# 89833
oComplete, Mini Protease Inhibitor Cocktail	Roche	Cat# 11836153001
Urea	Sigma-Aldrich	U5378
HisPur Ni-NTA Resin	ThermoScientific	Cat# 88221
Strep-Tactin XT 4Flow Resin	IBA Lifesciences	Cat# 25010002
Mini-Protean TGX Precast gel	Bio-Rad	4561085
InstantBlue Coomassie Protein Stain	Abcam	Ab119211
WesternBright Quantum	Advansta	K-12042
DMEM	Invitrogen	31600–034
Fetal bovine serum premium	RD Biosciences	S11150
Lipofectamine 3000	Invitrogen	Cat# L3000015

REAGENT or RESOURCE	SOURCE	IDENTIFIER
jetOPTIMUS	Polyplus	Ref# 101000006
Cytochalasin D	Sigma-Aldrich	C8237
EGTA	EMD Millipore	324626
Thapsigargin	Molecular Probes	T-7458
GeneJET Plasmid Miniprep Kit	ThermoScientific	K0503
NEBuilder HiFi DNA Assembly Master Mix	New England Biolabs	Cat# E2621
Q5 High-Fidelity DNA Polymerase	New England Biolabs	M0491G
EcoRI-HF	New England Biolabs	R3101S
KpnI-HF	New England Biolabs	R3142S
DpnI-HF	New England Biolabs	R0176S
Critical commercial assays		
Quick Start Bradford 1x dye reagent	Bio-Rad	5000205
Experimental models: Cell lines		
Madin-Darby canine kidney (MDCK) GII	James Nelson Lab, Stanford University	N/A
Oligonucleotides		
DNA primers, see Table S1	This study	N/A
Recombinant DNA		
ABLIM2	Harvard PlasmID	HsCD00347266
CRIP1	Harvard PlasmID	HsCD00325884
CRIP2	Harvard PlasmID	HsCD00347309
PDLIM1	Harvard PlasmID	HsCD00322576
PDLIM7	Harvard PlasmID	HsCD00041079
EPLINa	Addgene	Plasmid# 40947
pEGFP-C1-EPLINa LIM	Addgene	Plasmid# 40950
pmEmerald-C1-LASP1	Addgene	Plasmid# 54141; RRID:Addgene_54141
ISL1	Harvard PlasmID	HsCD00336822
LMO1	Harvard PlasmID	HsCD00346015

REAGENT or RESOURCE	SOURCE	IDENTIFIER
LIMK1	Harvard PlasmID	HsCD0036096
ZNF185	Harvard PlasmID	HsCD00462341
MICAL1	Harvard PlasmID	HsCD0033898
pEGFP-C1-PXN	Gift from Dr. Christopher Turner	N/A
pmEmerald-C1-PINCH	Addgene	Plasmid# 54229; RRID:Addgene_54229
FHL2	Harvard PlasmID	HsCD00326523
pEGFP-C1-ZYX	Gift from Dr. Masahiro Sokabe	N/A
pEGFP-C1-ZYX-LIM	Gift from Dr. Masahiro Sokabe	N/A
TRIP6	Gift from Dr. Dannel McCollum	N/A
Keratin 8	Addgene	Plasmid# 18063; RRID:Addgene_18063
mEmerald-Keratin 18	Addgene	Plasmid# 54134; RRID:Addgene_54134
C1-F-tractin-mCherry	Addgene	Plasmid #155218; RRID:Addgene_155218
Software and algorithms		
ImageJ	ImageJ	https://imagej.net/ij/
Microsoft Excel	Microsoft	N/A
PlotsofData	Universiteit van Amsterdam	https://huygens.science.uva.nl/PlotsOfData/
KaleidaGraph	Synergy Software	https://www.synergy.com
GraphPad Prism 10	GraphPad Software	https://www.graphpad.com/scientific-software/prism/
SlideBook	Intelligent Imaging Innovations	https://www.intelligent-imaging.com/slidebook?gad_source=1&gclid=EAIaIQobChMI_Lfa1aephAMVWs3CBB1FMQyiEAAYASAAEgKDOvD_BwE
Other		
Glass Bottom Dish	Cellvis	D35-20-1.5-N
Joystick Extreme 3D Pro	Polyplus	Ref# 101000006
3-axis 3D Micromanipulator	Physik Instrumente	M-110.1DG
P-97 Mercury DC-motor Controller Micropipette Puller	Sutter Instrument	C-862.00

REAGENT or RESOURCE	SOURCE	IDENTIFIER
Flaming/Brown Micropipette Puller	Sutter Instrument	Model P-97
Borosilicate glass rod: OD 1mm, length 15cm	Sutter Instrument	BR-100-15
Micropoint Laser Ablation system	Photonics Instrument	2205
Nitrogen pulse laser 337nm	Photonics Instrument	337-USAS
Coumarin 440 laser dye	Exciton	04400